

A radiomics-based study for differentiating parasellar cavernous hemangiomas from meningiomas.

Chunjie Wang

Department of Radiology, The Second Hospital of Dalian Medical University, Dalian

Lidong You

Department of Radiology, Taihe County People's Hospital, Taihe

Xiyou Zhang

Department of Radiology, The Second Hospital of Dalian Medical University, Dalian

Yifeng Zhu

Department of Radiology, The Second Hospital of Dalian Medical University, Dalian

Li Zheng

Department of Radiology, Jining NO. 1 People's Hospital, Jining

Wangle Huang

Department of Radiology, The First Affiliated Hospital of Wenzhou Medical University, Wenzhou

Dongmei Guo

Department of Radiology, The Second Hospital of Dalian Medical University, Dalian

Yang Dong (✉ 23121546@qq.com)

Department of Radiology, The Second Hospital of Dalian Medical University, Dalian

Article

Keywords: Radiomics, Parasellar, Cavernous Hemangioma, Meningiomas, Magnetic Resonance Imaging

Posted Date: April 7th, 2022

DOI: <https://doi.org/10.21203/rs.3.rs-1508602/v1>

License:  This work is licensed under a Creative Commons Attribution 4.0 International License.

[Read Full License](#)

Abstract

To investigate the value of the radiomic models for differentiating parasellar cavernous hemangiomas from meningiomas and to compare the classification performance with different MR sequences and classifiers. A total of 96 patients with parasellar tumors (40 cavernous hemangiomas and 56 meningiomas) were enrolled in this retrospective multiple-center study. Radiomics features were extracted from five MRI sequences using radiomics software. Three feature selection methods and six classifiers were evaluated in the training cohort to construct favorable radiomic machine-learning classifiers. The performance of different classifiers was evaluated using the AUC and compared to neuroradiologists. The detection rates of T₁WI, T₂WI, and CE-T₁WI for parasellar cavernous hemangiomas and meningiomas were approximately 100%. In contrast, the ADC maps had the detection rate of 18/22 and 19/25, respectively, (AUC, 0.881) with 2.25 cm as the critical value diameter. Radiomics models with the SVM and KNN classifiers based on T₂WI and ADC maps had favorable predictive performances (AUC > 0.90 and F-score value > 0.80). These models outperformed neuroradiologists (AUC, 0.756 and 0.545, respectively). Radiomic models based on T₂WI and ADC and combined with SVM and KNN classifiers have the potential to be a viable method for differentiating parasellar hemangiomas from meningiomas. T₂WI is more universally applicable than ADC values due to its higher detection rate for parasellar tumors.

Introduction

Parasellar cavernous hemangioma is a relatively rare extracerebral vascular malformation. Its detection rate has increased with the widespread use of magnetic resonance (MR)^{1–3}. Due to its relatively low incidence and lack of awareness among physicians, the clinical misdiagnosis rate for parasellar cavernous hemangioma is as high as 66.7–87.5%^{4,5}, and it is often misdiagnosed as parasellar meningioma^{6–9}. The treatment strategies for parasellar cavernous hemangioma and meningioma are different. The current standard treatment for parasellar hemangiomas is stereotactic radiosurgery (SRS), such as Gamma Knife and Cyber Knife. This technique is effective in reducing the lesion size, lowering the chance of extensive bleeding or nerve injury during surgery, and attaining long-term tumor control^{10,11}. However, the efficacy of SRS for meningiomas is relatively limited due to the increased risk of adhesions to surrounding tissues. Resection is considered to be an effective strategy for the treatment of parasellar meningiomas, and SRS can be used as an adjuvant treatment for postoperative residual or recurrent meningiomas^{12–14}. Consequently, accurate preoperative differentiation between parasellar cavernous hemangioma and meningioma is crucial for individualized treatment decisions.

Given their rarity, it is difficult for radiologists to accurately differentiate cerebellar cavernous hemangiomas from the relatively common meningiomas. MR imaging (MRI) helps to distinguish between parasellar cavernous hemangiomas and meningiomas^{15–17}. However, the morphological parameters and signal characteristics in MR images are nonspecific and subject to individual interpretation, resulting in a high level of inter-observer variability and misdiagnosis rate. In recent years, advanced functional imaging features have provided additional information to improve diagnostic

accuracy, including a description of compactness of tumor cell arrangement, cerebral blood perfusion, and vascular proliferation characteristics. Previous studies have shown that meningiomas have a significantly lower minimum apparent diffusion coefficient (min ADC) and significantly higher cerebral perfusion compared to cavernous hemangiomas. However, the ADC value is not yet universally applicable in clinical applications^{16,18}. The inherent low signal-to-noise ratio and magnetic susceptibility artifacts on diffusion-weighted imaging (DWI) are unavoidable, especially for small tumors. In addition, different types of meningiomas have been found to have different perfusion profiles, with the highest cerebral blood flow (CBF) values for angiomatic meningioma and the lowest for fibrous meningiomas.

Identification by perfusion status is typically incomplete¹⁹. Xiao et al. have reported that type B cavernous hemangiomas with arteriovenous shunt had high CBF values and were easily misdiagnosed as meningiomas²⁰. Dynamic contrast-enhanced MRI (DCE-MRI) has been used for the angiogenic evaluation of tumors. Its gradual “filling” features help in the diagnosis of cavernous hemangioma. However, the homogenous enhancement features of type A cavernous hemangiomas are similar to those of most meningiomas, which compromises the diagnosis. Moreover, injection of exogenous contrast agents is unavoidable, which limits their use in specific populations^{18,20,21}. Most advanced functional MRI techniques have been designed and applied in small groups, decreasing their generalizability. Therefore, their applicability in the differential diagnosis of parasellar cavernous hemangioma and meningioma still needs further validation.

Radiomics has become an attractive technique in recent years. It is a powerful tool for constructing decision-support models based on conventional or functional imaging for extracting large amounts of image features and quantitative data analysis²². However, there are limited data on radiological features as a means of differentiating parasellar cavernous angiomas from meningiomas. The present study extracted a large panel of radiomics features from T1-weighted images (T₁WI), T2-weighted images (T₂WI), contrast-enhanced T1-weighted images (CE-T₁WI), diffusion-weighted imaging (DWI), and apparent diffusion coefficient (ADC) imaging data involving 96 patients with parasellar cavernous hemangiomas and meningiomas. The study aimed to construct an MRI-based radiomics model as a noninvasive preoperative prediction method to facilitate the differentiation of parasellar cavernous hemangiomas from meningiomas.

Materials And Methods

Patients

Radiological and clinical databases of 96 cases of parasellar cavernous hemangiomas and meningiomas from Second Hospital of Dalian Medical University, Jining NO. 1 People's Hospital, and First Affiliated Hospital of Wenzhou Medical University were retrospectively reviewed between January 2010 and September 2019. This retrospective study was approved by the ethics review board of Second Hospital of Dalian Medical University, Jining NO. 1 People's Hospital, and First Affiliated Hospital of Wenzhou Medical University. The requirement for informed consent was waived by our Review Board

(Second Hospital of Dalian Medical University, Jining NO. 1 People's Hospital, and First Affiliated Hospital of Wenzhou Medical University) owing to the retrospective nature of the current study. The methods in the current study were performed in accordance with the relevant guidelines and regulations. Inclusion criteria included the following: (1) patients pathologically confirmed and/or clinically diagnosed with parasellar cavernous hemangioma or meningioma; (2) preoperative multi-parametric MRI scans including T₁WI, T₂WI, CE-T₁WI, DWI, and ADC data were acquired; and (3) patients with no history of preoperative treatment. Patients were excluded if (1) clinical data were incomplete; (2) they received any treatment before MRI examination, and (3) MR image quality was suboptimal. As a result, 40 cases of parasellar cavernous hemangiomas and 56 cases of parasellar meningiomas were included in the study. The flowchart for patient selection is presented in Fig. 1.

MR image acquisition and data management

MR examinations were performed in 37 and 59 patients using 1.5T (HDXT, GE Healthcare, USA) and 3.0T (Siemens, Verio, Germany) MR scanners, respectively. The MR scan parameters are summarized in Table 1. CE-T₁WI was acquired after administration of 0.1 mmol/kg of gadolinium-based contrast material (Gadovist; Bayer, Leverkusen, Germany). Diffusion-weighted images were transferred to a post-processing workstation to obtain ADC maps. MR data for T₁WI, T₂WI, and CE-T₁WI were acquired for all patients. DWI was obtained for 27 patients with cavernous hemangiomas and 32 patients with meningiomas. ADC maps were obtained for 22 patients with cavernous hemangiomas and 25 patients with meningiomas. All T₁WI, T₂WI, DWI, ADC, and CE-T₁WI data were selected for texture analysis.

Tumor segmentation

The radcloud platform (Huiying Medical Technology Beijing Co., Ltd, <http://radcloud.cn>) was used to manage the imaging and clinical data and to perform subsequent radiomics statistical analysis. All lesions in the training set were manually delineated by a junior radiologist on contiguous T₂WI slices and then copied to the corresponding T₁WI, CE-T₁WI, DWI, and ADC maps for each slice. The first and last image layers were excluded to reduce the partial volume effect in all of the following series. The volume of interest (VOI) was manually adjusted to avoid interference from magnetic sensitivity artifacts. A senior radiologist with 10 years of experience reviewed all contour lines and decided on the tumor boundaries when no consensus was reached. Next, the computer automatically generated a three-dimensional VOI. Both radiologists were double-blinded to both clinical and pathological information. Figure 2 depicts a schematic of the radiomics workflow.

Feature extraction and selection

A total of 1,409 quantitative imaging features were extracted from MR images using the Radcloud platform²³. All of these features were classified into four categories^{22,24}. (1) First order statistic: these features quantitatively described the intensity distribution of voxels in MR images, but did not involve the spatial arrangement of voxels. (2) Shape-based: these features reflected the shape of the depicted region.

(3) Texture: texture analysis quantified the variation of features within gray levels and described the statistical information related to the spatial distribution of gray levels or voxel intensities. This analysis was generally performed by second- or higher-order statistical methods that quantified the heterogeneity within the lesion. These features included Gray Level Run Length Matrix, (GLRLM), Gray Level Co-Occurrence Matrix (GLCM), and Gray Level Size Zone Matrix, (GLSZM). (4) High order features: high order features were obtained using statistical methods after filtering the images. They included Laplacian of Gaussian, Wavelet, Square, Square Root, and Logarithm.

In order to avoid over-fitting and improve the generalization ability of the model, variance threshold, select K best, and LASSO algorithm were used to select the optimal features (Fig. 3). A variance threshold of 0.8 was used in the variance threshold method to remove variance eigenvalues smaller than 0.8. The select K best was chosen to remove features without a statistically significant difference ($p > 0.05$). For the LASSO model, the L1 regularizer was used as the cost function with a cross-validation error value of 5 and a maximum number of iterations of 1,000. The LASSO algorithm was used to find the best alpha in each sequence, calculate the coefficients, and obtain the most relevant features.

Model training and validation

The present study constructed radiomics-based models using KNN, SVM, LR, RF, XGBoost, and DT classifiers. The radiomic features after a three-dimensional dimensionality reduction were used as the dataset. Then, 80% of the datasets were randomly selected to build the training set and the remaining 20% were used as the validation set to evaluate the accuracy of the models.

Neuroradiologist evaluation

Subsequently, two neuroradiologists (with 5 and 10 years of experience, respectively) made a diagnosis based on the characteristics of parasellar cavernous hemangiomas and meningiomas in conventional MR images (T₁WI, T₂WI, and CE-T₁WI), including morphology, size, signal intensity, and enhancement characteristics. Signal intensities were recorded according to the Elster scoring criteria¹⁷. The lesion diameters detected by ADC maps, T₂WI, and other sequences were recorded. The two neuroradiologists were blinded to the clinical and pathology data.

Statistical analysis

The present study compared and analyzed the area under the receiver operating curve (ROC) curve with 95% confidence interval (CI), sensitivity, specificity, and accuracy of each classifier based on the results of different MR sequence tests. Model stability was evaluated using the F-score value. The larger the F-score value, the better the stability of the model. The lesion detection rate on different MR images was also analyzed, and the relationship between lesion diameter and the detection rate on ADC maps was statistically evaluated using the SPSS 22.0 software (SPSS, Inc, Chicago, IL). Long-distance cut-off values for the Yoden index findings were obtained based on the data sensitivity and specificity. The

performance of the two neuroradiologists was evaluated using ROC curve analysis and compared to the performance of the final radiomics models.

Results

Clinical and MRI characteristics

Baseline characteristics of 96 patients are reported in Table 2. All lesions were detectable on conventional MR images (Fig. 4), with a mean diameter of approximately 2.66 ± 1.01 cm. The detection rate was 18/22 for cavernous hemangiomas and 19/25 for meningiomas on ADC maps. The area under the curve (AUC) for the detection rate was 0.881 (95% CI 0.790–0.972), with an accuracy, sensitivity, and specificity of 74.2%, 67.3%, and 100%, respectively (Fig. 5a). The mean diameter was approximately 2.74 ± 0.98 cm, with a critical value of 2.25 cm for the diameter on ADC maps.

The AUCs for the two neuroradiologists were 0.756 (95% CI 0.654–0.858) for reader 1 (Fig. 5b) and 0.545 (95% CI 0.430–0.659) for reader 2 (Fig. 5c). When comparing diagnostic performance, the radiomics classifier had a significantly higher AUC than the two neuroradiologists ($p < 0.001$).

Model assessment

After three-dimensionality reductions, eight out of 1,409 features were selected based on T₂WI (Table 3). Features based on other sequences are listed in Supplementary Tables S1–S4.

The diagnostic performance of the prediction models is summarized in Tables 4–5. After removing all over-fitting results for recognizable lesions, the T₂WI-based radiomics model with KNN and SVM classifiers was more effective in identifying parasellar cavernous hemangiomas from meningiomas (Fig. 6).

Discussion

The present study established an accurate classifier to distinguish parasellar cavernous hemangiomas from meningiomas by integrating a large panel of radiomic features. An efficient classifier was obtained by comparing five MRI sequences from 1.5 T and 3.0 T MR scanners at three medical imaging centers, bolstering its generalizability. The MRI-based radiomic classifier outperformed the neuroradiologists in terms of diagnostic accuracy, sensitivity, and specificity.

Radiomics can provide additional metabolic and biological information in addition to the traditional MRI metrics. Gray contrast, uniformity, depth, and texture roughness have been used to study tumor grading, prediction of genomic information, and differentiation of lesion and non-lesion images^{25–27}. The present study found that higher-order features could better reflect the degree of tumor heterogeneity and texture information. A GLSZM can quantify gray-level zones in an image to reflect tumor heterogeneity at a local

scale. The coefficient of High Gray-Level Zone Emphasis was the largest, which measured the distribution of the higher gray-level values. Larger values indicated a larger proportion of high gray-level values and size zones in the image²⁸. Tumor heterogeneity usually reflected the gray contrast variation of the image. Therefore, the GLSZM was more sensitive in distinguishing parasellar cavernous hemangiomas from meningiomas.

The present study focused on the inadequacy of visual examination in differentiating parasellar cavernous hemangiomas from meningiomas in order to assess the clinical role of radiomics in facilitating and enhancing visual analysis by radiologists. T₂WI and ADC sequences had a good practical value in constructing radiomics models. T₂WI was characterized by a high signal-to-noise ratio, homogeneity, and significant hyperintensity^{16,29}. The radiomics model constructed based on T₂WI had a high diagnostic accuracy and stability in distinguishing parasellar hemangiomas and meningiomas. Radiomics models based on ADC maps were equally valuable in the differential diagnosis when parasellar hemangiomas and meningiomas were identified. However, the detection rate of lesions in ADC maps was about 78.7%. Contrary to our general view, the accuracy of the radiomics model based on CE-T₁WI was low, although it was improved in different ways. This might be influenced by different types of cavernous hemangiomas and meningiomas^{30–32}.

The present study compared the detection rates for parasellar cavernous hemangiomas and meningiomas obtained using different MRI sequences, which has not been attempted in previous studies. The detection rate of DWI and ADC maps was 78.7% (37/47), with a cut-off diameter of 2.25 cm. The detection rate of T₂WI, T₁WI, and CE-T₁WI was 100%, which was more conducive to the establishment of radiomics models.

Different classifier algorithms may lead to different results. The present results suggested that the radiomics models combined with SVM and KNN classifiers had better diagnostic performance in distinguishing between parasellar cavernous hemangiomas and meningiomas. SVM has been proposed by Cortes et al. in 1995 as a binary classifier based on supervised learning^{33,34}. The critical concept of SVM involves the use of a hyperplane to define decision boundaries to separate different classes of data points. This technique finds support vectors with a high discrimination and maximizes the interval between classes. It has good adaptability and discrimination ability. The K-nearest neighbor (KNN) method is mostly used for image classification. This object classification is based on the distance between its neighbors and is mainly used to solve regression and classification problems. By selecting the KNN points of a sample when the nearest neighbors belong to a certain category, the sample is determined to belong to that category. Several previous studies have demonstrated KNN's excellent and stable performance using different datasets, which was similar to the present result^{35–37}. Consistent with our study, other classifiers also suffer from over-fitting. This is manifested by the fact that the training set is too accurate, while the validation set cannot achieve the expected ideal results. In addition, there are too many feature dimensions, parameters, and noise, which lead to a too-perfect prediction of the fitted function in the training set. However, the prediction results in the new data test set were low. In the present

study, SVM and KNN classifiers were suggested for use as radiological diagnostic models to distinguish between parasellar cavernous hemangiomas and meningiomas.

There are several limitations in the present study. First, the sample size was relatively small and needs to be further explored. Second, different types of parasellar cavernous hemangiomas and meningiomas were not considered. Third, the differential diagnosis mainly focused on parasellar hemangiomas and meningiomas. Other parasellar tumors that are relatively easy to diagnose were not included in the study.

In conclusion, the proposed T₂WI-based radiomics model combining SVM and KNN classifiers showed favorable predictive efficacy in the preoperative differential diagnosis between parasellar cavernous hemangiomas and meningiomas. It had more general applicability in complementing conventional imaging modalities and as an alternative to functional imaging. Moreover, the more readily available T₂WI could provide higher detection rates and more texture features. Other imaging modalities based on T₂WI for differentiating parasellar cavernous hemangiomas and meningiomas need to be explored.

References

1. Linskey M, et al. Cavernous sinus hemangiomas: a series, a review, and an hypothesis. *Neurosurgery*.**30**(1),101–108(1992).
2. Biondi A, et al. Intracranial extra-axial cavernous (HEM) angiomas: tumors or vascular malformations? *Journal of neuroradiology = Journal de neuroradiologie*.**29**(2),91–104(2002).
3. Del Curling O, et al. An analysis of the natural history of cavernous angiomas. *Journal of neurosurgery*.**75**(5),702–708(1991).
4. Lombardi D, et al. Sellar and parasellar extra-axial cavernous hemangiomas. *Acta neurochirurgica*.**130**,47–54(1994).
5. Hasiloglu Z, et al. Cavernous hemangioma of the cavernous sinus misdiagnosed as a meningioma: a case report and MR imaging findings. *Clinical imaging*.**37**(4),744–746(2013).
6. Phi J, et al. Intracranial capillary hemangioma: extra-axial tumorous lesions closely mimicking meningioma. *Journal of neuro-oncology*.**109**(1),177–185(2012).
7. Mansour T, et al. The Art of Mimicry: Anterior Clinoid Dural-Based Cavernous Hemangioma Mistaken for a Meningioma. *World neurosurgery*.**100**,708.e719-708.e722(2017).
8. Buchbender C. Meningioma and associated cavernous hemangioma as a parasellar tumor. *Neurosurgical review*.**11**(2),201–203(1988).
9. Lan Z, et al. A giant solid cavernous hemangioma mimicking sphenoid wing meningioma in an adolescent: A case report. *Medicine*.**97**(44),e13098(2018).
10. Lee C, et al. Gamma Knife radiosurgery for hemangioma of the cavernous sinus. *Journal of neurosurgery*.**126**(5),1498–1505(2017).
11. Wang X, et al. Hypofractionated stereotactic radiosurgery: a new treatment strategy for giant cavernous sinus hemangiomas. *Journal of neurosurgery*.**128**(1),60–67(2018).

12. Sindou M, et al. Cavernous sinus meningiomas: imaging and surgical strategy. *Advances and technical standards in neurosurgery*.**42**,103–121(2015).
13. Tripathi M, et al. Safety and efficacy of single-fraction gamma knife radiosurgery for benign confined cavernous sinus tumors: our experience and literature review. *Neurosurgical review*.**43**(1),27–40(2020).
14. Hafez R, et al. Stereotactic Gamma Knife surgery safety and efficacy in the management of symptomatic benign confined cavernous sinus meningioma. *Acta neurochirurgica*.**157**(9),1559–1564(2015).
15. Nadarajah J, et al. MR imaging of cavernous sinus lesions: Pictorial review. *Journal of neuroradiology = Journal de neuroradiologie*.**42**(6),305–319(2015).
16. Shah R, et al. Key imaging characteristics for preoperative identification of cavernous sinus hemangioma. *Radiology case reports*.**10**(1),1013(2015).
17. Elster A, et al. Meningiomas: MR and histopathologic features. *Radiology*.**170**,857–862(1989).
18. Zhou W, et al. Magnetic resonance imaging diagnosis and microsurgical treatment of cavernous sinus hemangiomas. *Acta Academiae Medicinae Sinicae*.**35**(6),677–682(2013).
19. Lu Y, et al. The role of three-dimensional pseudo-continuous arterial spin labelling in grading and differentiating histological subgroups of meningiomas. *Clinical radiology*.**73**(2),176–184(2018).
20. Xiao H, et al. The role of magnetic resonance diffusion-weighted imaging and three-dimensional arterial spin labelling perfusion imaging in the differentiation of parasellar meningioma and cavernous haemangioma. *The Journal of international medical research*.**42**(4),915–925(2014).
21. Yao Z, et al. Magnetic resonance imaging characteristics with pathological correlation of cavernous malformation in cavernous sinus. *Journal of computer assisted tomography*.**30**(6),975–979(2006).
22. Yip S, et al. Applications and limitations of radiomics. *Physics in medicine and biology*.**61**(13),R150–166(2016).
23. Wu J, et al. Radiomics and radiogenomics for precision radiotherapy. *Journal of radiation research*.**59**,i25-i31(2018).
24. Gillies R, et al. Radiomics: Images Are More than Pictures, They Are Data. *Radiology*.**278**(2),563–577(2016).
25. Takahashi S, et al. Radiomics Analysis for Glioma Malignancy Evaluation Using Diffusion Kurtosis and Tensor Imaging. *International journal of radiation oncology, biology, physics*.**105**(4),784–791(2019).
26. Park Y, et al. Radiomics and machine learning may accurately predict the grade and histological subtype in meningiomas using conventional and diffusion tensor imaging. *European radiology*.**29**(8),4068–4076(2019).
27. He K, et al. Magnetic resonance standard for cavernous sinus hemangiomas: proposal for a diagnostic test. *European neurology*.**72**,116–124(2014).

28. Zwanenburg A, et al. The Image Biomarker Standardization Initiative: Standardized Quantitative Radiomics for High-Throughput Image-based Phenotyping. *Radiology*.**295**(2),328–338(2020).
29. Montoya F, et al. Cavernous Sinus Hemangioma: Imaging Diagnosis and Surgical Considerations. *World neurosurgery*.**146**,e30-e37(2021).
30. Jinhu Y, et al. Dynamic enhancement features of cavernous sinus cavernous hemangiomas on conventional contrast-enhanced MR imaging. *AJNR American journal of neuroradiology*.**29**(3),577–581(2008).
31. Yadav R, et al. Imaging characteristics of cavernous sinus cavernous hemangiomas. *The neuroradiology journal*.**25**(5),515–524(2012).
32. Lin B, et al. Correlation between magnetic resonance imaging grading and pathological grading in meningioma. *Journal of neurosurgery*.**121**(5),1201–1208(2014).
33. K K, et al. An Efficient Method for Brain Tumor Detection Using Texture Features and SVM Classifier in MR Images. *Asian Pacific journal of cancer prevention: APJCP*.**19**(10),2789–2794(2018).
34. Cortes C, et al. Support-vector networks. *Machine Learning*.**20**,10(1995).
35. Demirhan A. The effect of feature selection on multivariate pattern analysis of structural brain MR images. *Physica medica: PM : an international journal devoted to the applications of physics to medicine and biology : official journal of the Italian Association of Biomedical Physics (AIFB)*.**47**,103–111(2018).
36. Jiang S, et al. An Improved k-Nearest Neighbor Algorithm for Text Categorization. *Expert Systems with Applications*.**39**(1),1503–1509(2003).
37. Demirhan A. Neuroimage-based clinical prediction using machine learning tools. *International Journal of Imaging Systems and Technology*.**27**(1),89–97(2017).

Tables

Table 1

MRI protocol.

Sequences	TR (ms)	TE (ms)	NEX	Slice Thickness (mm)	FOV (mm)	Matrix
SE-T ₁ WI	1750–2500	9–25	2-4	3–5	24 × 24	256 × 256
FSE-T ₂ WI	4000–4500	90–120	2	3–5	24 × 24	256 × 256
DWI	4500–6400	70–80	2	3–5	24 × 24	256 × 256

Label: SE = spin echo, FSE = fast spin echo, TR = repetition time, TE = echo time, NEX = number of excitations, FOV = field of view, DWI = diffusion-weighted imaging.

Table 2

Baseline characteristics and distribution of the population study.

Characteristics	All Patients (n = 96)	cavernous hemangioma (n = 40)	Meningiomas (n = 56)	t/χ ²	p Value
Age(y)	58.14 ± 12.02 (23–86)	56.20 ± 14.05 (23–86)	59.52 ± 10.10 (26–80)	7.708	0.186
Sex				0.649	0.420
Men	27/96 (0.28)	13/40 (0.33)	14/56 (0.25)		
Women	69/96 (0.72)	27/40 (0.67)	42/56 (0.75)		

Table 3

Description of selected radiomic features with their associated feature group and filter based on T₂WI.

Radiomic feature	Radiomic class	Filter
Median	firstorder	Lbp-2D
InterquartileRange	firstorder	wavelet-LLL
Variance	firstorder	wavelet-LLL
Skewness	firstorder	original
Skewness	firstorder	gradient
HighGrayLevelZoneEmphasis	glszm	wavelet-LHL
LargeDependenceHighGrayLevelEmphas	glcm	wavelet-HLL
Skewness	firstorder	wavelet-LHL

Label: GLDM = Gray-Level Dependence Matrix, GLSZM = Gray-level Size Zone Matrix.

Table 4

Performance of KNN classifier radiomics models in differentiating parasellar cavernous hemangiomas from meningiomas in the validation set.

Label: MRI: magnetic resonance imaging; T₁WI: T₁-weighted images; T₂WI: T₂-weighted images; DWI: diffusion-weighted images; CE-T₁WI: contrast-enhanced T₁-weighted images; AUC: areas under the ROC curves; 95% CI: 95% confidence interval.

Table 5

Performance of SVM classifier radiomics models in differentiating parasellar cavernous

MRI sequence	Category	AUC	95%CI	sensitivity	specificity	F-Score
T ₂ WI	meningiomas	0.93	0.78–1.00	0.92	0.88	0.9
	Cavernous hemangioma	0.93	0.78–1.00	0.88	0.92	0.88
ADC	meningiomas	0.93	0.75–1.00	0.88	1	0.89
	Cavernous hemangioma	0.93	0.75–1.00	1	0.88	0.89
CE-T ₁ WI	meningiomas	0.92	0.69–1.00	0.82	0.71	0.82
	Cavernous hemangioma	0.92	0.69–1.00	0.71	0.82	0.71
DWI	meningiomas	0.79	0.56–1.00	0.5	1	0.67
	Cavernous hemangioma	0.79	0.56–1.00	1	0.5	0.80
T ₁ WI	meningiomas	0.75	0.55–0.94	0.83	0.75	0.83
	Cavernous hemangioma	0.75	0.55–0.94	0.75	0.83	0.75

hemangiomas from meningiomas in the validation set.

MRI sequence	Category	AUC	95%CI	sensitivity	specificity	F-Score
T ₂ WI	meningiomas	0.87	0.71–1.00	0.92	0.88	0.92
	Cavernous hemangioma	0.87	0.71–1.00	0.88	0.92	0.88
ADC	meningiomas	0.95	0.77–1.00	0.88	1	0.89
	Cavernous hemangioma	0.95	0.77–1.00	1	0.88	0.89
CE-T ₁ WI	meningiomas	0.91	0.73–1.00	1	0.71	0.92
	Cavernous hemangioma	0.91	0.73–1.00	0.71	1	0.83
DWI	meningiomas	0.94	0.71–1.00	0.67	1	0.80
	Cavernous hemangioma	0.94	0.71–1.00	1	0.67	0.86
T ₁ WI	meningiomas	0.73	0.52–0.94	0.75	0.75	0.78
	Cavernous hemangioma	0.73	0.52–0.94	0.75	0.75	0.71

Label: MRI: magnetic resonance imaging; T₁WI: T₁-weighted images; T₂WI: T₂-weighted images; DWI: diffusion-weighted images; CE-T₁WI: contrast-enhanced T₁-weighted images; AUC: areas under the ROC curves; 95% CI: 95% confidence interval.

Figures

Figure 1

Flowchart for patient selection.

Figure 2

Radiomics workflow.

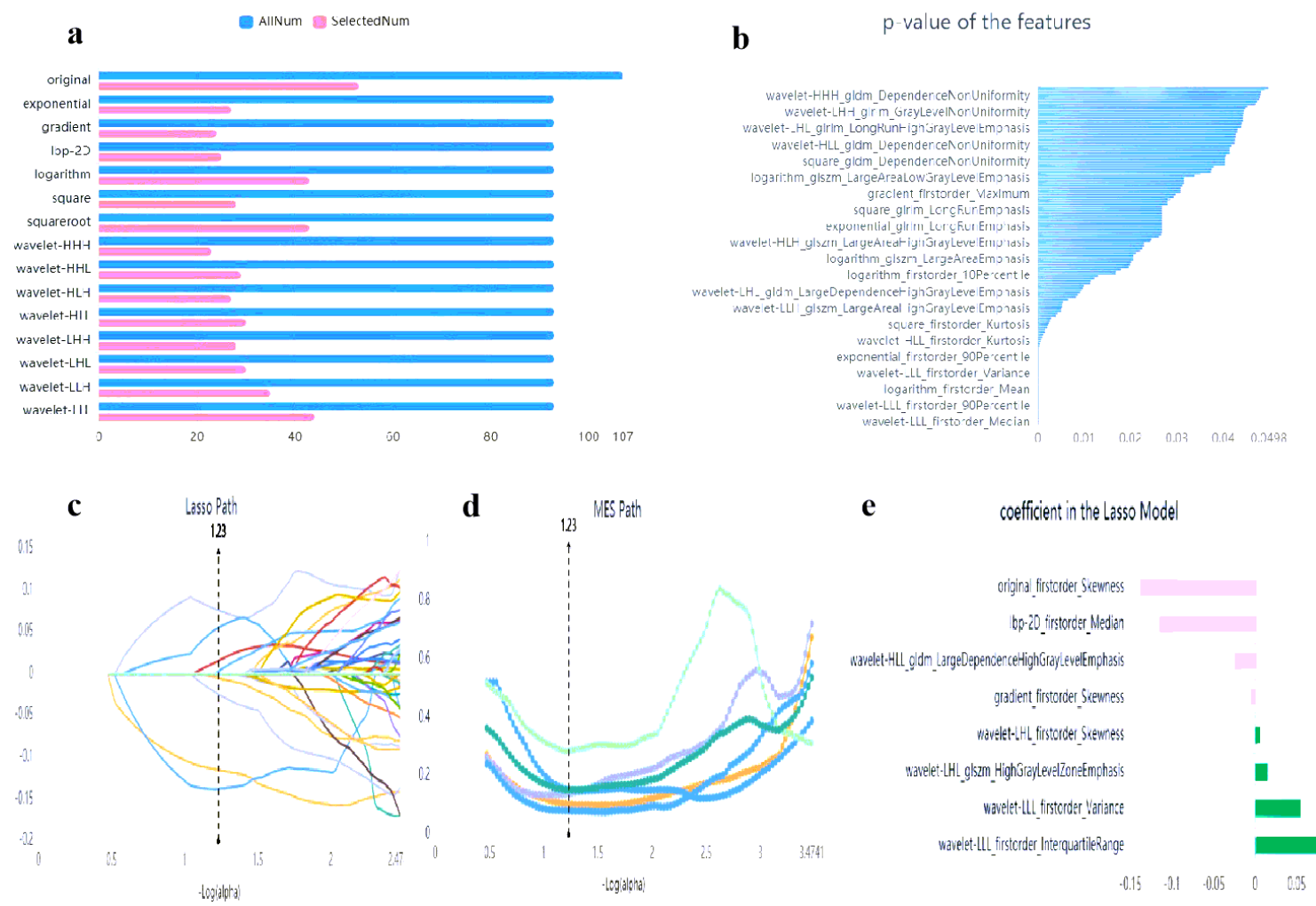


Figure 3

Dimension reduction analysis and feature selection for T₂WI. Variance threshold method was used to select 486 features from 1,409 radiomics features (variance threshold=0.8); b. 145 features were retained using select K best (p value<0.05); c-e. 145 features were retained using LASSO algorithm method. Eight eigenvalues were retained.

Figure 4

a–e Images of parasellar cavernous hemangioma in a 75-year-old woman. f–j Images of parasellar meningioma in a 58-year-old woman. MRI protocol included a, f axial T2-weighted images, b, g, axial T1-weighted images, c, h diffusion-weighted images, d, i apparent diffusion coefficient maps, and e, j contrast-enhanced T1-weighted images. Cavernous hemangioma exhibited high signal intensities on T2-weighted images, low signal intensities on T1-weighted images, DWI, and ADC map, and CE-T₁WI showed heterogeneous enhancement. Meningioma exhibited slightly high signal intensities on T2-weighted images, slightly low signal intensities on T1-weighted images, DWI, and ADC map, and CE-T₁WI showed homogeneous enhancement.

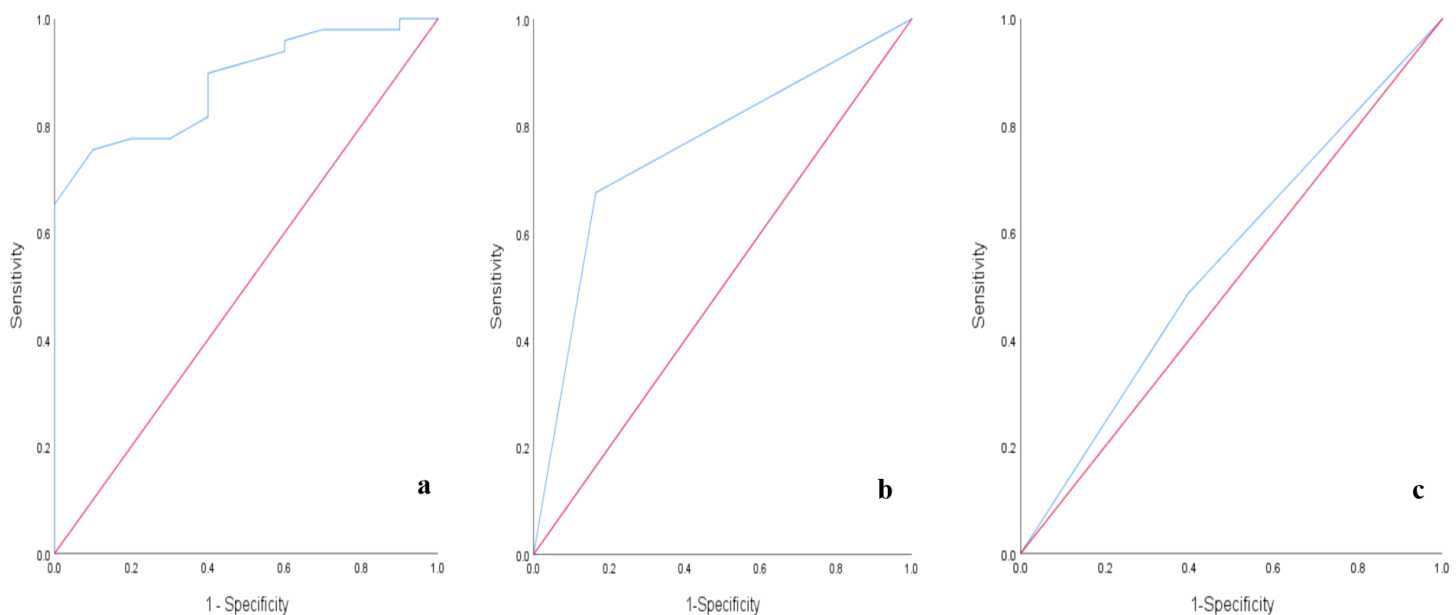


Figure 5

Receiver operating characteristic (ROC) curves of ADC map detection rate (a, AUC=0.881) and diagnostic efficiency of two neuroradiologists (b, AUC=0.756; c, AUC=0.545).

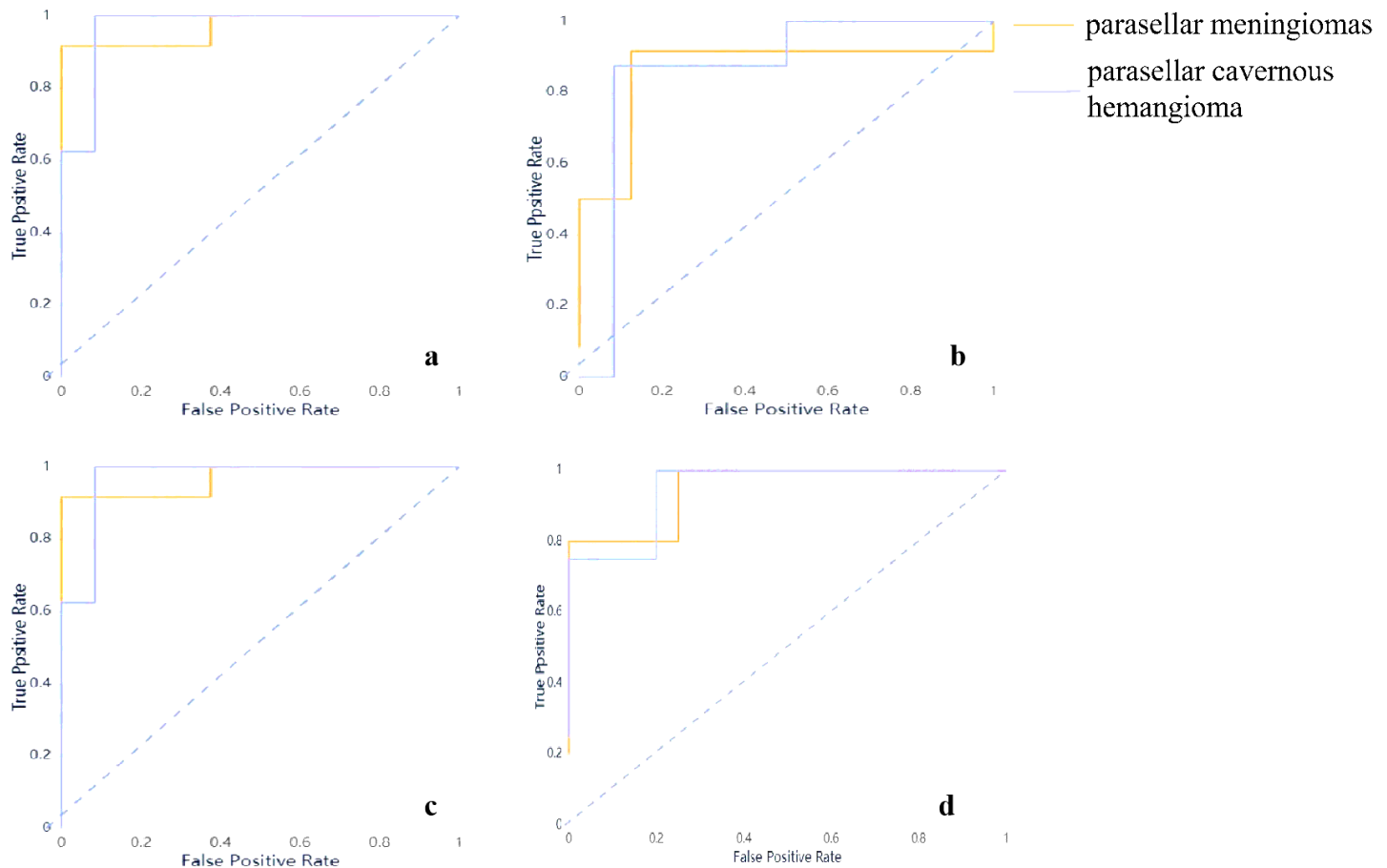


Figure 6

ROC curves for the optimal classifier. a. ROC curve for KNN model based on T_2 WI with AUC=0.93; b. ROC curve for SVM model based on T_2 WI with AUC=0.88; c. ROC curve for KNN model based on ADC maps with AUC=0.83; d. ROC curve for SVM model based on ADC maps with AUC=0.81.

Supplementary Files

This is a list of supplementary files associated with this preprint. Click to download.

- [SupplementaryMaterial.docx](#)